Geomech. Geophys. Geo-energ. Geo-resour. (2026) 12:58
https://doi.org/10.1007/s40948-025-01044-z

RESEARCH

Exploring the brittle behavior of 3D-printed sandstone analogs under various stress conditions

Dima Shamsedine · Pooya Hamdi · Sergey Ishutov · Gonzalo Zambrano-Narvaez · Angel J. Sanchez-Barra · Lisa Winhausen · Rick J. Chalaturnyk · Florian Amann

Received: 27 November 2024 / Accepted: 4 September 2025

Abstract Rock masses essentially consist of two components: the intact rock and spatially distributed rock joints of various orientations and persistence. The first step to characterize the behavior of a rock mass is to understand the strength and deformability of the intact rock by performing repetitive destructive laboratory tests on intact rock specimens. The challenge imposed in these tests is the existence of inherent microscopic heterogeneity, which can lead to a substantial variability. 3D printing technologies, specifically the binder jetting technique using sand and furan, has been recently adopted in studies of rock analogs due to its ability to produce synthetic sedimentary rocks with complex geometries and known characteristics, and reduced variability. For a synthetic material to be used as an analog for a natural brittle rock, it is essential to demonstrate that this analog exhibits brittle behavior similar to that of natural rocks. Although there have been several recent advancements in 3D printing applications in the geomechanics field, studies that thoroughly evaluate the 'brittle' behavior aspects of rock analogs are lacking. In this study, a set of requirements is established to evaluate the brittle behavior of the 3D-printed rock analogs, derived from uniaxial and triaxial compression, Brazilian, and fracture toughness laboratory tests, including the tensile and compressive strengths, crack initiation and crack damage thresholds, stiffness, and brittle-ductile transition. Analysis of laboratory test results showed that the analogs behaved similar to moderately-to-strong natural sandstones with a UCS in the range of 28–32 MPa and tensile strength of 5–6 MPa, with an acceptable repeatability among the test results. Under triaxial loading, the failure process was dominated by extensional fracturing at low confinement with a transition to a macroscopic shear failure mode at higher confining pressures (up to 15 MPa). At confining pressure beyond the Mogi line, compaction failure occurred indicating a typical brittle to ductile transition, which is corroborated by microstructural analyses.

D. Shamsedine (✉) · P. Hamdi · L. Winhausen · F. Amann
Department of Engineering Geology and Hydrogeology, RWTH Aachen University, Lochnerstrasse 4-20, 52064 Aachen, Germany
e-mail: shamsedine@lih.rwth-aachen.de

S. Ishutov
Department of Environmental and Physical Sciences, Concordia University of Edmonton, Edmonton, AB T5B 4E4, Canada

G. Zambrano-Narvaez · A. J. Sanchez-Barra · R. J. Chalaturnyk
Department of Civil & Environmental Engineering, University of Alberta, Edmonton, AB T6G 1H9, Canada

F. Amann
Research Institution for Energy Infrastructure and Geothermal Systems, IEG, Kockerellstrasse 17, 52062 Aachen, Germany

Published online: 24 February 2026

Keywords Additive manufacturing · 3D printed synthetic sandstone · Rock mechanics testing · Brittle materials · And fracture mechanics

Abbreviations

AE	Acoustic emission
ASTM	American society for testing and materials
BJP	Binder jetting printing
BTS	Brazilian test
CD	Crack damage threshold
CI	Crack initiation threshold
COD	Crack opening displacement
CoV	Coefficient of variation
CT	Computed tomography
DIC	Digital image correlation
FT	Fracture toughness
3DP	3-Dimensional -printing
GSI	Geological strength index
HB	Hoek-brown criterion
LVDT	Linear variable differential transformer
MC	Mohr-coulomb criterion
NDT	Non-destructive testing
SCB	Semi-circular bend test
SEM	Scanning electron microscopy
TRX	Triaxial compression test
TSA	Test series A
TSB	Test series B
UCS	Uniaxial compressive strength

1 Introduction

Many studies have shown that the failure of brittle rocks is often dominated by development of extensional fractures rather than shear fractures, particularly when the rocks are subjected to zero or low confining pressure (Bieniawski 1967b, 1967a; Brace & Bombolakis 1963; Cook 1965; Hoek 1968; Hoek & Bieniawski 1965; Horii & Nemat-Nasser 1985; Martin 1997; Tapponnier & Brace 1976). Laboratory results revealed that the fracturing process in brittle rocks can be divided into four main regions including: crack closure, elastic stage, stable crack growth, and unstable crack growth (Bieniawski 1967a; Eberhardt 1998; Martin 1997). These regions can be identified either by direct visual observation techniques; i.e., optical or scanning electron microscopy (SEM), or X-ray based imaging techniques (Fonseka et al. 1985; Tapponnier & Brace 1976, Nasseri et al. 2011; Zhang et al. 2020), or by using a number of non-destructive testing techniques (NDT) including strain measurement and acoustic emission monitoring (Diederichs et al. 2004; Eberhardt 1998; Eberhardt et al. 1999; Martin 1993).

Figure 1 shows typical stress–strain curves together with Acoustic Emission (AE) monitoring data for a cylindrical sample under unconfined compression. The crack closure stage is characterized by closure of pre-existing cracks (Bieniawski 1967b). The stress–strain behavior in this stage is non-linear, exhibiting an increase in axial stiffness (i.e. Young's modulus) (Eberhardt 1998). The crack closure stage is followed by linear elastic deformation in which the elastic constants of the rock; i.e., Young's modulus and Poisson's ratio can be calculated. Crack initiation represents the stress level where micro-fracturing begins and is identified as the point where the lateral and volumetric strain curves depart from linearity. Crack growth in this stage is stable implying that crack extension is a function of loading and can be controlled (Bieniawski 1967b). In AE monitoring technique, crack initiation is identified as the first point at which a systematic increase in acoustic emissions occurs. In-situ observations and laboratory testing have shown that crack initiation typically begins at a stress level corresponding to 30–50% of the uniaxial compressive strength (UCS) (Eberhardt et al. 1998; Scholz 1968; Martin 1997; Martin & Chandler 1994). The stable crack growth continues until the unstable crack growth threshold is reached. The onset of unstable crack growth (crack damage threshold) is considered to be the point where the stress–axial strain curve deviates from linearity and/or at which the reverse in volumetric strain occurs. This stress level is identified from AE data by a significant increase in AE counts. The unstable crack growth continues to the point at which various microcracks merge to form larger cracks and the rock can no longer support an increase in the load (peak strength).

The first step to characterize the behavior of a rock mass is to understand the strength and deformability of the intact rock. This is often done by carrying out a series of mechanical laboratory testing including uniaxial/triaxial compression test, direct shear test, and direct/indirect tension test on "intact" samples (i.e., samples that do not contain macroscopic, visible, open joints, or other weakness planes). Some key characteristics of rocks such as compressive

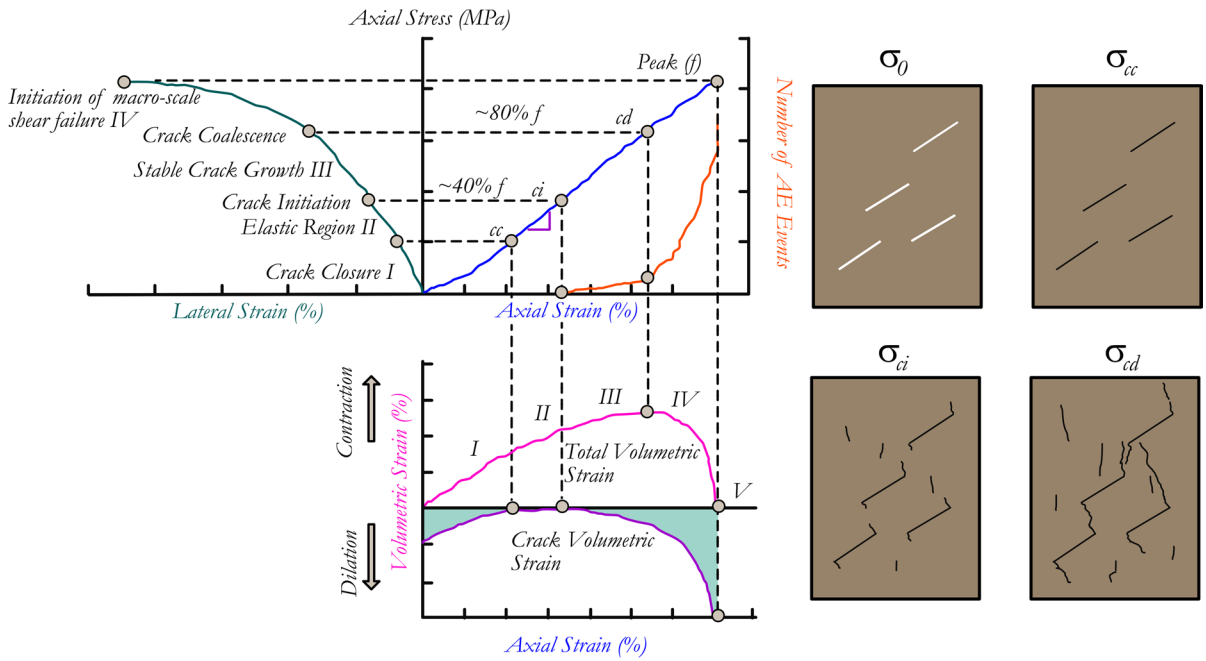

Fig. 1 Schematic illustration of the various stages of brittle failure under unconfined compression stress (modified after Cai et al. 2004)

strength, crack initiation (CI) and crack damage (CD) thresholds can be defined through the analysis of the stress–strain response and the micro-acoustic emission during compressive strength tests. One of the main challenges in analyzing such laboratory tests is often related to the quantification of rock properties due to a significant variability in test results, mainly associated with inherent, microscopic heterogeneity within the specimens (Bewick et al. 2015, 2019). At the laboratory scale, heterogeneity can be divided into three types: mineral heterogeneity, microcrack heterogeneity, and fracture networks (Lan et al. 2010; Amann et al. 2014; Ündül et al. 2015). Regardless of the type, the spatial distribution of these heterogeneities is extremely difficult to characterize prior to laboratory tests, imposing an inherent natural variability in the testing results. Bewick et al. (2015, 2019) showed that the intact unconfined compressive strength of a macroscopical intact and homogeneous rock could have a Coefficient of Variation (COV) > 25%. As a consequence of this variability in intact rock strength, it is difficult to quantify factors that could affect the rock mass strength, particularly the strength-degrading effect of non-persistent discontinuities.

Here, we discuss the application of 3D-printed, synthetic rock samples to overcome challenges associated with heterogeneities in natural rock samples and present the laboratory test results on "intact" rock analogs that produce behavior similar to natural materials with a very low variability (Primkulov et al. 2017). Fulfilling such a requirement is a first step to understand the complex behavior of a rock mass at the laboratory scale.

2 3D printing technology in geomechanics

According to the American Society of Testing Material (ASTM 2015), Additive Manufacturing, also known as 3D printing, can be categorized into seven methods, depending on the material and the machine technology used. The Binder Jetting Printing (BJP) technique involves selective deposition of a binder onto the powder layers, bonding the grains together to form a solid part. The process is repeated one layer at the time until the final geometry is created. The materials commonly used in the BJP include metals, sand, and ceramics that appear in granular form. Using silica sand as a core material, it is possible to create a

synthetic sandstone that behaves similar to a natural rock under various loading conditions i.e., compression and tension (Primkulov et al. 2017; Perras & Vogler 2018; Gomez et al. 2018). Using BJP technique, it is possible to print discrete fracture networks with predefined geometries, including non-persistent discontinuities, inside the printed volumes. This ability is demonstrated by Hamdi and Amann (2020), in which a non-persistent penny-shaped fracture is printed within a cylindrical sample and then fracture is detected in Computed Tomography (CT) scanning through visual inspection of CT images.

Recent advancements in the field of 3D printing (3DP) have been adopted in various scientific fields including geomechanics (Fereshtenejad and Song 2016; Vogler et al. 2017; Primkulov et al. 2017). The primary advantage of using 3D printing in laboratory experiments is to minimize the level of uncertainty and variability inherited from the heterogeneous nature of natural rock samples, making the geomechanical testing repeatable.

Using the binder jetting printing technique specifically, Zhang & Li (2022) studied the effect of the freezing and thawing phenomena on high porosity rock replicas, Aad et al., (2023) examined the effect of different factors on the aperture and closure of a rock joint during direct shear testing on rock replicas, and further demonstrated the ability of BJP to replicate artificial rock joints behaving similarly to low-strength natural rocks (<10 MPa). Gomez et al. (2018) investigated the suitability of 3D-printed silica sand samples in reproducing the geomechanical and flow characteristics of a natural sandstone at the laboratory scale and demonstrated the capability of the 3D-printed sandstone analog in reproducing the behavior of the natural sandstone.

Primkulov et al. (2017) studied the impact of thermal curing on the strength of 3D-printed samples composed of sand and furfuryl alcohol resin-based binder. Their results showed that the uniaxial compressive strength of 3D-printed samples could be increased by subsequent thermal curing and could reach up to 19 MPa. Vogler et al. (2017) compared the indirect tensile strength of a 3D-printed sandstone with several natural sandstones by carrying out Brazilian tests. They concluded that the 3D-printed samples exhibited tensile strength, surface roughness, and crack propagation characteristics of a weak natural sandstone. Perras and Vogler (2018) examined various geomechanical characteristics of 3D-printed sandstone including uniaxial compressive strength, stiffness, crack initiation, and crack damage threshold and showed the suitability of the artificial sandstone in replicating natural rocks.

More recently, additional studies have broadened the scope of 3DP in rock mechanics. Tian et al. (2023) carried out uniaxial, triaxial, and tensile tests on sand-based 3D-printed rock-like samples and concluded that the mechanical properties of the specimens can be reliably tailored by adjusting printing parameters, demonstrating their potential as synthetic rock analogs. Niu et al. (2023) provided a comprehensive review on the applications and prospects of 3D printing in rock mechanics and engineering, highlighting its advantages in controllability, reproducibility, and potential for embedding fracture networks. (Zhuang et al. 2024) investigated parameter regulation in rock-like samples and emphasized that curing temperature, binder content, and layer thickness have a strong influence on strength and deformation, providing insight into optimizing the printing process.

In this study, we explore the capability of the Binder Jetting Printing as an analog for brittle geomaterials. The mechanical characteristics (i.e., strength and deformation) of various 3D-printed samples are examined and compared to natural brittle rocks and other replicas including resin based, cement based, and gypsum rock analogs. We establish the following requirements (R1 to R5) to assess whether the 3D-printed rock analogs behave similar to natural brittle rocks:

The strength in compression is similar to typical sedimentary rocks (e.g., sandstone).
The ratio between UCS and Young's modulus falls in the domain of natural brittle rocks according to the ISRM classification (Ulusay 2015).
The brittle damage thresholds are consistent with natural rocks, i.e. crack initiation threshold occurring at around 30–50% of the UCS and crack damage at around 70–90% of the UCS (Bieniawski 1967b).
The ratio between tensile strength and UCS is in the range of 1/30 – 1/5.
The failure process changes from an extensional fracture-dominated mode at low confinement, to a macroscopic shear failure mode at high con-

finements, and the brittle to ductile transition is defined by the Mogi Line (Mogi 1966).

Upon fulfilling the above requirements, the rock analogs can be used for more advanced studies, if the variability (i.e. in many natural rocks $\geq 20\%$) is significantly reduced, i.e. less than 10%.

3 Methodology

3.1 Sample printing process

To evaluate the geomechanical behavior of sandstone analogs, a series of cylindrical and disk-shape specimens were printed using BJP with Ex-One M-FLEX system (Ex-One 2014), located in the GeoPrint facility at University of Alberta. The strength of the 3D-printed sandstone depends on various parameters including the grain types, grain size distribution, binder type and saturation, printing orientation, and layer thickness, which in this study are similar to those used by (Primkulov et al. 2017). The binding liquid (ExOne FB001), composed primarily of furfuryl alcohol, was applied to silica sand with a particle size distribution of D10, D50, and D90 of 110, 175, and 220 µm, respectively. The sand powder was deposited in 250 µm layers using a vibrating hopper moving at a constant recoating speed of 200 mm/s and a fixed height of 6 mm above the powder bed. The binder was dispensed as a directed cloud of microdroplets from a print head with 4×256 piezoelectric nozzles, applied in closely spaced parallel lines to achieve uniform bonding between layers. Upon completion of printing, all specimens were placed in an oven at 80 °C for 24 h for thermal curing. The dimensional accuracy of the printed specimens was within $\pm 0.5\%$ (e.g., ± 0.5 mm for a 100 mm specimen).

The printing orientation is the angle between the layering direction (i.e., printing direction) and the applied load. In the UCS and Brazilian tests, the printing orientation is parallel to the applied load (Fig. 2a, b) and in the fracture toughness test, the printing orientation is perpendicular to the applied load (Fig. 2c).

The binder saturation is defined as the percentage in volume of void spaces filled by Furfuryl alcohol. A higher binder saturation results in increasing the peak strength of the 3D-printed specimen; nevertheless, an excessive binder saturation could lead to the accumulation of the binder material at the bottom of the specimen which results in a heterogeneous binder distribution and strength along the specimen (Hodder et al. 2018).). In this study, two printing configurations (Test Series) with different binder saturation were selected to evaluate the capability of the 3D printing method in producing specimens with various strength and deformability characteristics. The level of repeatability for strength and deformation characteristics was evaluated by carrying out multiple tests with similar printing configurations. A list of all the specimens tested in this study is presented in Table 1. The binder saturation values listed in Table 1 are obtained by measuring the samples after they have been printed.

Prior to destructive testing, petrophysical tests were performed on a few samples in order to obtain basic properties of the synthetic rock. The average values of dry density, saturated density, and porosity were determined to be 1560 kg/m^3, 1925 kg/m^3, and 40% respectively, with a negligible ($< 5\%$) difference between both test series. The calculated porosity is 2–3 times higher than in natural sedimentary rocks, specifically sandstones (Burley & Kantorowicz 1986). Hodder et al. (2020, 2022) discussed several methods to decrease the porosity in the printed samples. The methods include choosing an optimum grain size distribution and grain morphology for the deposited powder, in addition to compacting every sand layer after its deposition on the printing bed using a roller. However, they showed that the high porosity created due to the round morphology of the sand grains is inevitable, since using angular grains would result in poor flowability of the powder during its deposition on the printing bed. All the mentioned methods are followed in the printing procedure of the analogs used in this study in order to obtain a minimal porosity of 40%.

3.2 Experimental setup

The uniaxial compression tests (UCS), Brazilian tests, and fracture toughness tests were carried out using a servo-controlled *Zwick* machine with a loading capacity of 100 kN. UCS cylindrical samples, 50*mm* in diameter and 100*mm* in height (H:D ratio of 2:1) were printed and tested (Fig. 2-a). The vertical

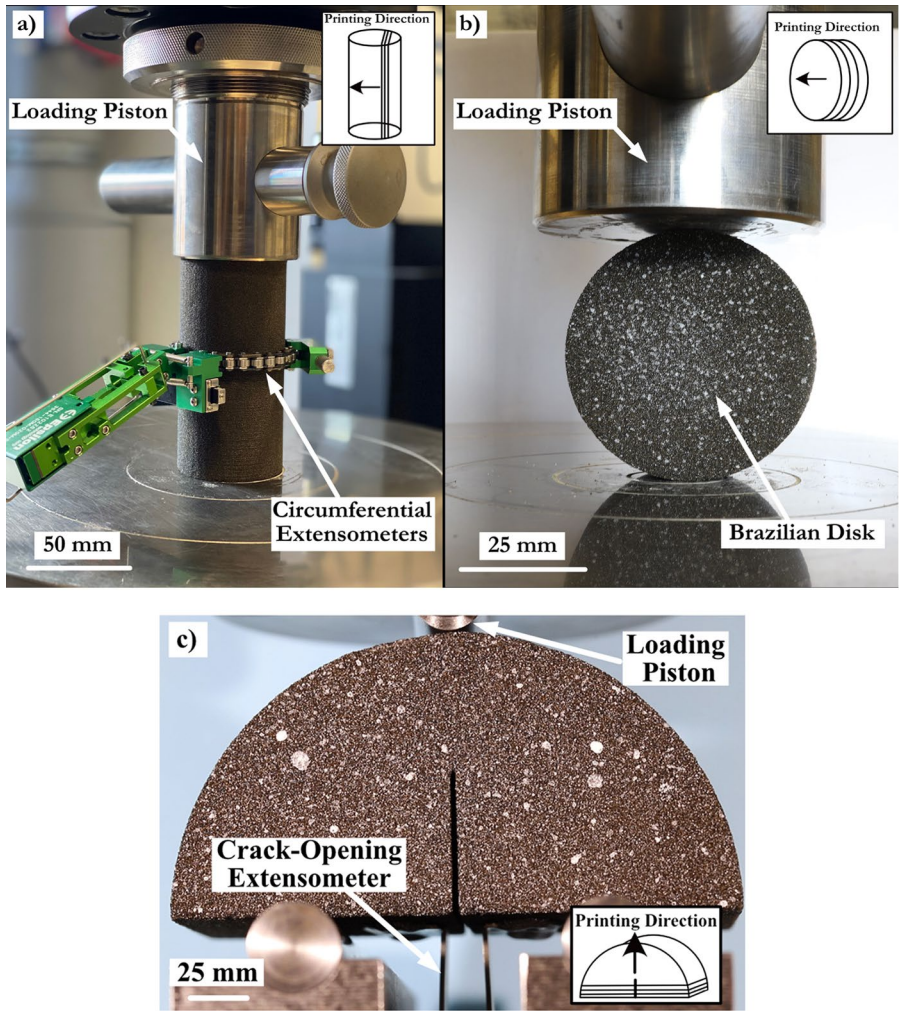

Fig. 2 Experimental set-up for **a** uniaxial compression test, **b** Indirect tension (Brazilian) test, **c** semicircular bending test

Table 1 The set of 3D-Printed samples tested in the study

	Binder saturation (%)	Uniaxial compression test (UCS)	Triaxial compression test (TRX)	Brazilian test (BTS)	Fracture toughness test (FT)
Test Series A (TSA)	14.5	5	10	6	-
Test Series B (TSB)	17.0	10	20	10	3

movement of the upper piston was used to calculate the axial strain. For the lateral strain measurement, an extensometer was attached to a chain wrapped around the sample. The uniaxial compression testing procedure recommended by ASTM (ASTM D7012, 2010) was followed. The UCS tests were carried out with an axial deformation rate of 0.05 mm/min.

Brazilian tests were carried out on disk-shape samples, 50 mm in diameter and 25 mm in thickness (T/D = 0.5) (Fig. 2-b). The BTS tests were performed using flat platens and the testing procedure was adopted according to the recommendation by ASTM (2021).

Fracture toughness tests were carried out, based on the ISRM suggested method ISRM (2014), on a semicircular bending (SCB) specimen having a radius and a thickness of 50 mm both. The pre-existing notch

length and width are 25 mm and 1 mm respectively. A crack opening extensometer was attached to the bottom of the sample as seen in Fig. 2-c to measure the crack mouth opening displacement during the test. Tests were displacement controlled using a velocity of 0.05 mm/min.

Digital Image Correlation (DIC) was utilized to assess the fracturing process of the synthetic samples under indirect tension (Brazilian Test and SCB tests). To increase the pixel contrast, white speckles were sprayed on the surface of the sample disks with an air-brush to create the desired random texture to improve the quality of DIC results. A digital *Canon 6D Mark II* camera with a frame rate of 50 fps was used to film Brazilian tests. A high-speed camera *Optronis Cyclone-25–150-M (Mono)* with a frame rate of 800 fps was used for filming the SCB tests. A fixed lighting condition was ensured in both cases. The DIC analysis was conducted using an open-source 2D digital DIC software *Ncorr* (Blaber et al. 2015).

A servo-electrical, triaxial rock testing machine with a maximum loading capacity of 100 kN was used to test the cylindrical printed samples, which were 30 mm in diameter and 60 mm in height (H:D ratio of 2:1). All specimens were placed in a 0.5-mm thick fluorocarbon jacket. On opposing sides of the specimens, three axial LVDTs (linear variable differential transformers) (Fig. 3), each with a measurement base-length of 50 mm, were firmly attached. A diametral extensometer was attached to the specimen at mid-height to measure the lateral displacement. A wide range of confining stresses from 0.2 to 15 MPa were selected to study the behavior of the 3D-printed samples under both low and higher confining pressures. An isostatic stress state was achieved by the simultaneous increase of both axial and radial stress components until the target confinement was reached. A constant axial displacement rate of 0.05 mm/min was applied to the top of the samples while the radial confining pressure was kept constant. All tests were manually stopped right after rupture to avoid extensive sample disintegration and to allow for an assessment of the failure characteristics.

3.3 Thin section method

Thin section analysis was conducted in this study to closely examine the microstructure of the rock analogs and to better understand the compactional failure mode occurring at the grain scale. After TRX and UCS tests, the cylindrical samples were subjected to epoxy resin stabilization to maintain their microstructure during further preparations. The stabilized sample is cut in half longitudinally, and a thin sliver is then cut out using a diamond saw. This sliver is ground until it's optically flat (30 µm) using progressively finer abrasive grit, treated with epoxy, and placed on top of a glass sheet. This process leads to rock analogs thin sections with length of 48 mm and width of 28 mm, allowing light to pass through, making them ready for viewing under a microscope.

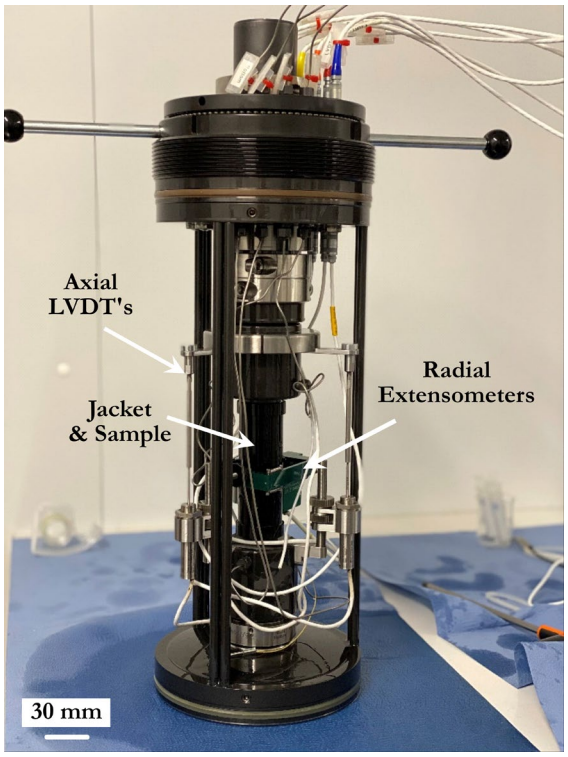

Fig. 3 Experimental set-up of the triaxial compression test

4 Laboratory results

4.1 Uniaxial compression test results

4.1.1 Stress–strain relationship

Figure 4 presents an example of the stress–strain curves obtained from uniaxial compression tests

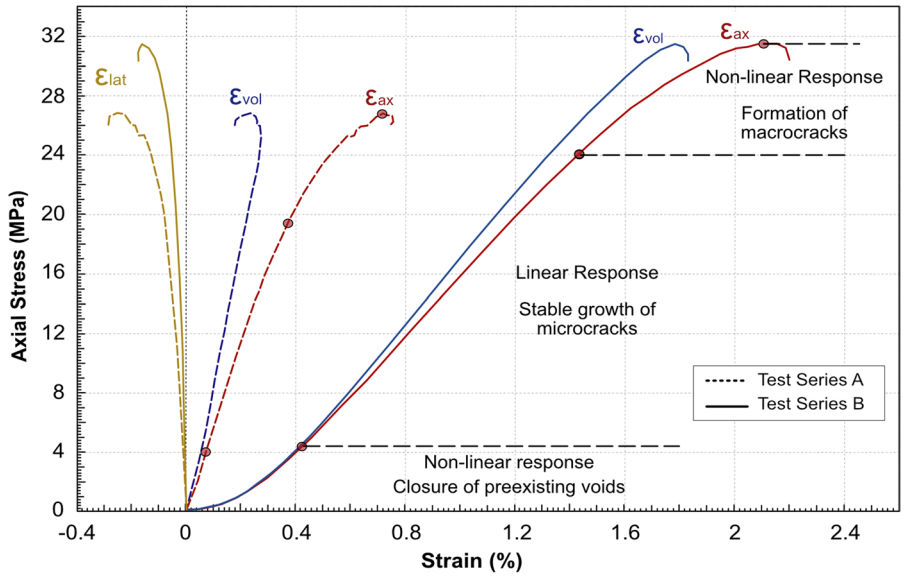

Fig. 4 Stress vs. strain curves obtained from uniaxial compression test on 3D printed synthetic samples (TSA and TSB), showing different stages of brittle fracturing

carried out on test series A (TSA) and test series B (TSB). Similar to natural brittle rocks, the results show an elastic brittle-plastic behavior for both test series, with a sudden post-peak stress drop. The axial stress–strain curve starts with a non-linear trend with increasing stiffness, indicating the compaction and/or closure of pre-existing voids in the sample. At higher axial stresses, the axial strain curve becomes linear enabling the determination of the Young's modulus (E). Upon further loading, the stress strain curves become progressively non-linear and eventually approach the peak bearing capacity (i.e. UCS).

There is a distinct difference between TSA and TSB stress–strain responses. The higher binder saturation in TSB (17% vs. 14.5%) led to higher uniaxial strength compared to TSA, demonstrating the possibility of producing samples with varied strength using the 3D printing method. In contrast, the axial strain at failure for TSA (i.e. 0.7% of total strain) is significantly lower than for TSB samples (i.e. 2.1% of total strain), showing a higher level of axial compaction in TSB. This resulted in absence of volumetric strain reversal prior to failure (i.e. typically observed for brittle rocks and TSA) in TSB.

4.1.2 Strength and stiffness properties

Perras & Vogler (2019) were able to prove that the use of sand and furan with the binder jetting technology is the most promising combination to produce a brittle rock-like synthetic material, but they reached a maximum UCS value of 7 MPa, which categorizes this material as a low-strength rock according to the ISRM strength classification. The UCS of the analogs in this study was 26 MPa and 32.5 MPa for TSA and TSB respectively, a factor 3–5 higher, due to a higher binder saturation and heat-curing. Despite the absolute magnitude of UCS, both TSA and TSB failed predominately through axial splitting commonly observed for natural brittle rocks under unconfined compression (Jaeger et al. 2007; Basu et al. 2013). The analogs (i.e. both, TSA and TSB samples) fulfill requirement R1 of the minimum UCS for a moderate strength rock. The Young's modulus calculated for TSA and TSB is 4.5 GPa and 2 GPa, respectively. The ratios (UCS/E) of TSA, TSB, and other rock analogs obtained from earlier studies on synthetic rocks (Perras and Vogler 2018; Salami 2021; Tatone 2014), are plotted in Fig. 5, and compared to the natural sedimentary rocks modulus ratio domain. Results show that the printing configuration used in this study produces synthetic sandstones that a) are on the lower limit of an average modulus ratio (TSA) or b) at the lower limit of low modulus ratio (TSB). The calculated coefficient of variation of the UCS test results is 3.3% and 12.3% for TSA and TSB respectively, indicating an acceptable inter-sample variation for TSA and relatively high inter-sample variation for TSB which will be discussed in Sect. 4.3.

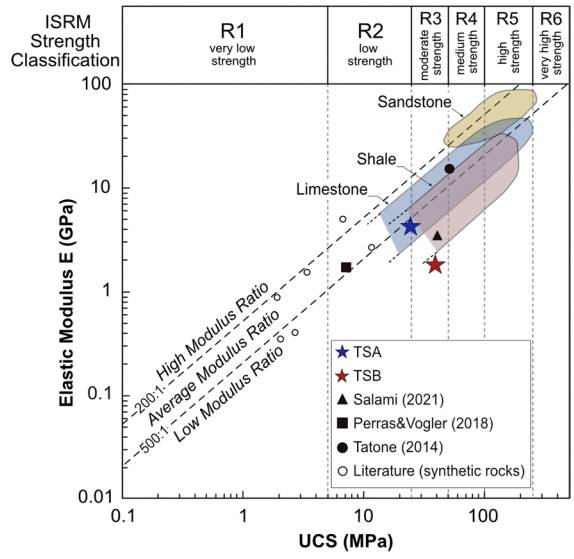

Fig. 5 The relationship between the Young's modulus and UCS for the current study (TSA and TSB) and published data on natural and synthetic rocks. Based on Deere & Miller (1966), modified from Tatone (2014)

4.1.3 Brittle damage thresholds

Extensive research has been conducted on natural rocks to determine damage thresholds such as the crack initiation (CI) and crack damage (CD) for various brittle rock types. It is shown that under unconfined compressive loading, CI typically occurs between 30–50% of UCS and CD at 70–90% of UCS. Several methods were suggested in earlier studies for determining damage thresholds based on the stress–strain curves recorded during compressive loading (Bieniawski 1967b; Diederichs et al. 2004; Martin 1993; Martin & Chandler 1994; Nicksiar & Martin 2013). In this study, the crack initiation is determined as the point where stress-lateral strain curve (ε_{lat}) deviates from linearity (Bieniawski 1967b; Brace et al. 1966; Lajtai & Lajtai 1974), and crack damage stress is determined as the point where stress-axial strain curve (ε_{ax}) deviates from linearity (Bieniawski 1967b; Lajtai & Lajtai 1974; Martin 1997).

Figure 6 shows an example of the method to derive the onset of CI and CD from lateral stress/strain and axial stress/strain curves, respectively. This method is used for all the corresponding stress–strain curves recorded by TSA and TSB and the mean values of the results are obtained.

The onset of the CI for both test series is estimated to be ~ 35% of UCS and the CD threshold at ~ 75% of UCS (Fig. 7). This agrees with findings from previous studies on brittle rocks such as sedimentary and crystalline rocks (Amann et al. 2011; Cai et al. 2004; Nicksiar & Martin 2013; Perras & Diederichs 2014; Perras & Vogler 2019, p. 201), demonstrating that the requirement R3 is fulfilled for both TSA and TSB samples. However, TSB samples do not show a volumetric strain reversal as typically observed for brittle rocks under uniaxial compression. The distinct onset of non-linearity in the axial strain curve at

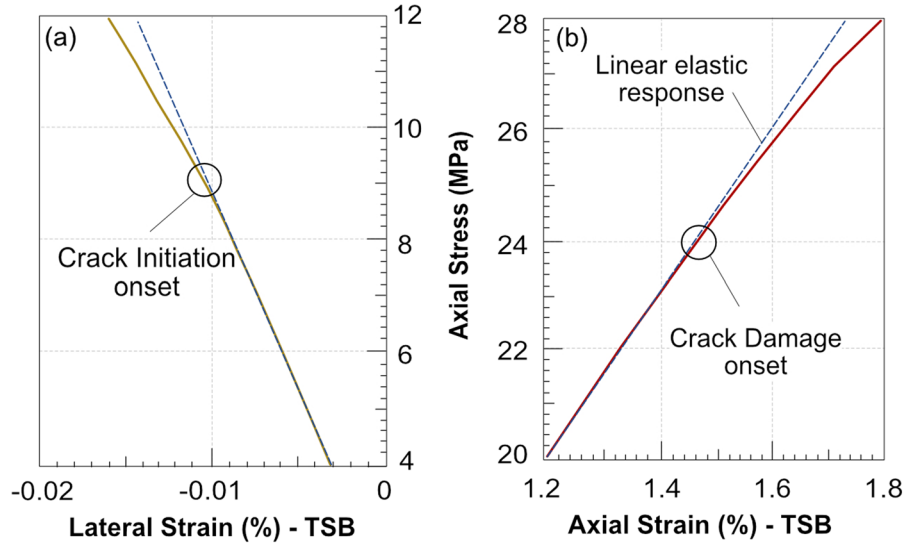

Fig. 6 An example of the method adopted for determining **a** the crack initiation threshold CI, and **b** the crack damage threshold CD, based on the deviation from linearity of the axial stress—strain curves obtained from a UCS test on TSB

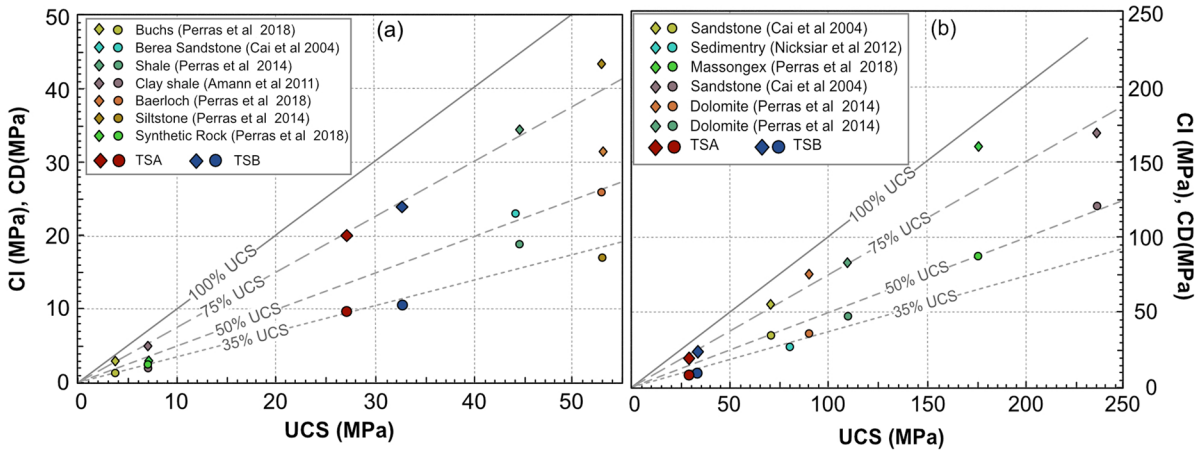

Fig. 7 UCS vs. CI (circular markers), and UCS vs. CD (diamond-shape markers) ratios plotted for the 3D printed rocks (TSA, TSB and Ex1-SF), and compared to other natural sedimentary rocks (listed in the legends). UCS ranges from 0 to 50 MPa in (a) and from 0 to 250 (MPa) in (b) to cover a wider range of UCS values

approximately 75% of UCS may indicate pronounced compaction failure rather than crack coalescence. For axial loads higher than CD, TSB samples show a volumetric compression rather than extension.

4.2 Brazilian test results

For each test series, 10 Brazilian tests were carried out to allow for calculating the variability of the results. The average indirect tensile strength was found to be 3.5 MPa for TSA and 5.6 MPa for TSB, with a standard deviation of 0.4 MPa and 0.7 MPa, respectively. The calculated coefficient of variation (CoV) is 10,7% and 11,6% for TSA and TSB, respectively. The validity of test results highly depends on the boundary conditions imposed in the experimental setup, therefore, digital image correlation (DIC) analysis was used to monitor the failure process and ensure that failure initiates in the disc's center and propagates towards the loading points to be considered valid (Li & Wong 2012; Mellor & Hawkes 1971). Figure 8 presents the ratio of UCS to tensile strength (strength ratio) of TSA and TSB along with data points from earlier studies on rock replicas (Perras & Vogler 2018; Salami 2021; Tatone 2014). Compared to other replica material, the sand-furan 3D-printed analogs used in this study have a tensile strength to UCS ratio of 1/5 to 1/10, and thus fall within the average strength ratio of sedimentary rocks, fulfilling requirement R4.

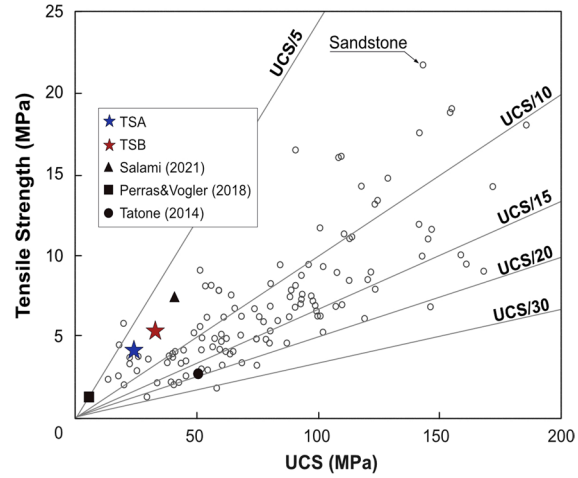

Fig. 8 The relationship between the tensile strength and UCS for the current study (TSA and TSB) and published data on natural and synthetic rocks modified from Tatone (2014)

4.2.1 Semi-circular bending test results

In his studies on natural rocks, Hoagland (1973) observed that the fracture development during a 3-point-bending test, as analyzed through the load-crack-opening-displacement (COD) curve, can be divided into three main regions: Region I, characterized by linear elastic behavior; Region II, marked by nonlinear inelastic pre-peak behavior with no visible crack extension; and Region III, where a decrease in

the applied load accompanies visible crack extension. A similar phenomenon was observed in the 3-point-bending tests on TSB rock analogs. The resulting load-COD curve, as shown in Fig. 9-a, also indicates three regions: the initial linear elastic behavior; the deviation from linearity at approximately 75% of the peak load, indicating the onset of inelastic behavior due to increasing microcracks above the notch, without visible crack extension; and the post-peak section, characterized by a slight load decrease followed by brittle failure, during which visible crack extension occurs, signifying the coalescence of microcracks. Digital image correlation analysis of the rock analog during the tests showed that—just before brittle failure occurring – a fracture process zone is developed above the notch with no visible crack, indicating a high strain intensity along the lateral axis due to formation of microcracks (Fig. 9-b).

The critical stress intensity factor, known as Mode I fracture Toughness K_{Ic}, is found to be 0.95 MPa. $m^{1/2}$, calculated from the peak load recording using Eq. 1 suggested by ISRM (Kuruppu et al. 2014):

$$K_{Ic} = Y' \frac{P_{max}\sqrt{\pi a}}{2RB} \quad (1)$$

where $Y\prime = -1.29 + 9.516\left(\frac{s}{2R}\right) - \left(0.47 + 16.457\left(\frac{s}{2R}\right)\right)\left(\frac{a}{R}\right) + \left(1.071 + 34.401\left(\frac{s}{2R}\right)\right)\left(\frac{a}{R}\right)^2$

a, *s*, *BandRarenotchlength*, *spanlength*, *samplethickness*, *andsampleradius*, *respectively*

The ratio $\frac{\sigma_t}{K_{Ic}}$ of the rock analog is 5.79, falling in an acceptable proximity from the empirical relation between tensile strength and fracture toughness deduced by Zhang (2002) during his studies on natural rocks: $\frac{\sigma_t}{K_{Ic}} = 6.88$.

4.3 Triaxial compression test results

4.3.1 Stress–strain relationship and brittle damage thresholds

Similar to natural sedimentary brittle rocks, triaxial compression tests on 3D-printed samples of TSA and TSB (Fig. 10) show that the peak strength increases with increasing confining pressure (Byerlee 1968; Jaeger et al. 2007), and the post peak behavior changes from brittle to ductile. At low confining pressures (i.e. < 1.5 MPa), the post-peak behavior is characterized by a sudden stress drop. At higher confining pressures (i.e. > 5 MPa), no evident post-peak stress drop is observed, indicating a typical ductile post-peak behavior. The TSB results however, exhibited some discrepancies caused by the non-uniformity of the strength among the rock analogs. Sanchez-Barra et al. (2023) studied the impact of position of the samples in the printing bed on the final strength of the samples and concluded that the strength and stiffness of the printed samples are influenced by their locations in the printing bed. The exhibited discrepancy in the TSB is attributed to this factor. The coefficient of variability can be further reduced by maintaining a consistent printing location for the rock analogs in the future printing jobs.

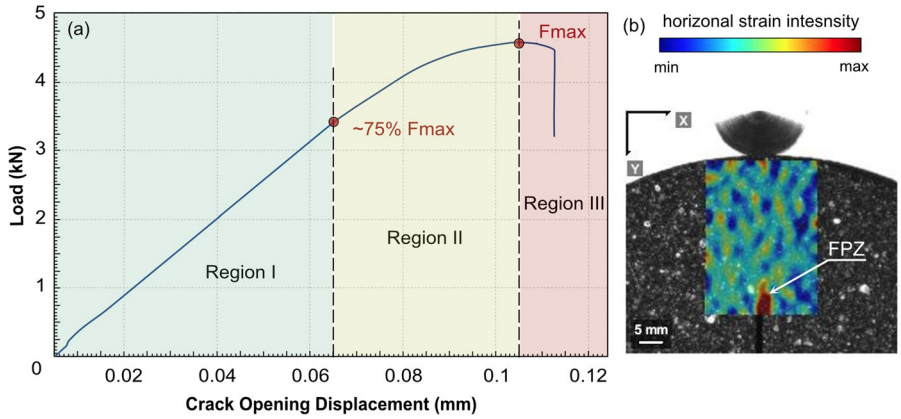

Fig. 9 Results of a 3-point-bending test on a semicircular 3D printed rock: **a** load-COD curve **b** horizontal strain field results captured just before failure using DIC analysis

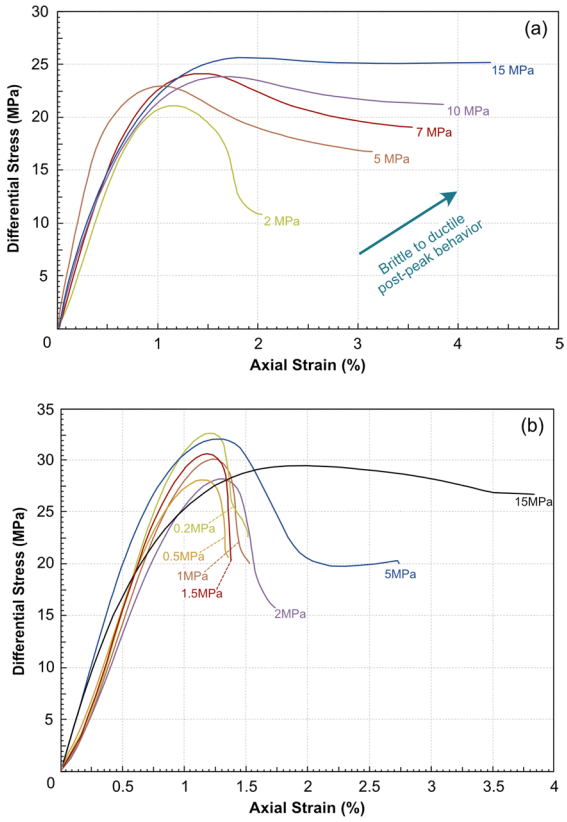

Fig. 10 Results of triaxial compression tests with various confining pressures on **a** TSA and **b** TSB

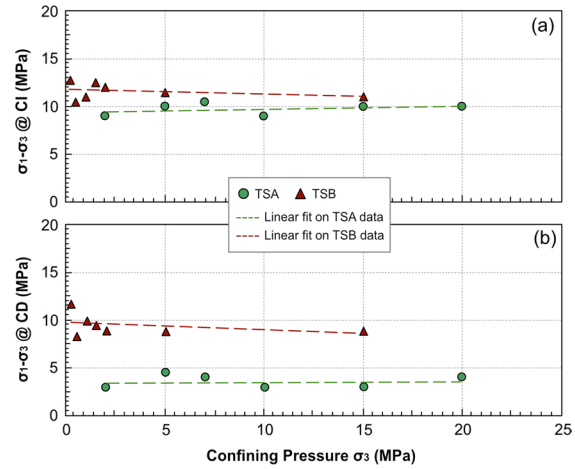

Fig. 11 Differential stress determined at which **a** the crack initiation and **b** the crack damage occurred in TSA and TSB at different confinement pressure values during TRX tests

To evaluate the impact of confining pressure on the brittle damage thresholds of the 3D-printed synthetic samples, the differential stress at crack initiation and crack damage obtained from various triaxial tests was calculated as a function of the confining pressure, and the results are presented in Fig. 11. The results of the TSA and TSB indicated that, while the peak strength increases with an increase in confining pressure, the brittle damage thresholds are almost independent of the confinement level, agreeing well with natural brittle geomaterials (Amann et al. 2012).

4.3.2 Strength properties

Triaxial and indirect tensile laboratory test results from this study were used to derive the Hoek–Brown (HB) and Mohr–Coulomb (MC) failure envelopes for each of the test series. Mogi (1966) studies revealed that there is a transition from brittle to ductile behavior in many rocks with increasing confining pressure. Mogi's line determines the boundary between brittle and ductile region at $\frac{\sigma_1}{\sigma_3} = 3.4$. Any test data lying to the right side of the Mogi line indicate that failure occurred in a ductile manner. This is consistent with the macroscopic appearance, i.e. no visible shear fracture, of TSB specimens at 15 MPa confining pressure (Fig. 12). The confining stresses at which the material fails in a ductile manner according to Mogi's line are 15 MPa for TSB and 10, 15, and 20 MPa for TSA (marked by a cross sign). These points are not included in the curve fitting, since the criterion is not applicable for compaction failure beyond Mogi's line (Bewick & Kaiser 2014).

The empirical HB criterion for intact rock samples is as follows:

$$\sigma_1 = \sigma_3 + \sigma_{ci}\left(m\frac{\sigma_3}{\sigma_{ci}} + s\right)^a \quad (2)$$

where σ_1 and σ_3 are the major and minor principal stresses at failure, respectively, σ_{ci} is the uniaxial compressive strength of the intact rock material and m, s and a are empirical constants. For the intact rock, the constant "a" is set to be 0.5. The RSData software (Rocscience Inc., 2007) was used for the curve fitting on the laboratory test results based on a Linear Regression algorithm to derive the HB material constant m_i. The MC envelope is derived by fitting a linear relationship to the data points plotting to the left of Mogi's line.

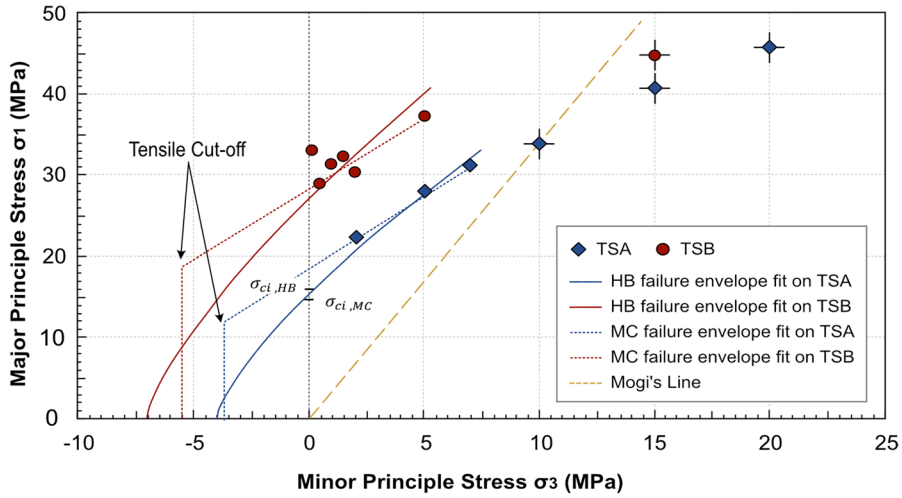

Fig. 12 MC and HB failure envelopes of the 3D printed synthetic sandstone fitted on the data sets obtained from UCS, TRX and Brazilian tests. Data points on the right side of Mogi line are indicated by a cross mark

Table 2 presents the Hoek–Brown and Mohr–Coulomb parameters derived from the curve fittings on laboratory results of the test series A and B. The m_i is calculated to be 3.6 which is relatively low compared to natural sandstones (Grasselli 2001; Hoek et al. 1998). The calculated cohesion for TSA and TSB is 7 and 11 MPa, respectively with friction angles of 16° (TSA) and 15° (TSB). Although the obtained UCS values fall within the range of natural sandstones with moderate strength, both the friction angles and mi values for both TSA and TSB samples are significantly smaller than typically observed for natural sandstones. Barton (1976) reports basic friction angles for natural sandstones ranging between 25° and 34°. Hoek and Brown (1997) suggest a mi value of 19 for natural sandstone.

The relatively low friction angles and mi values obtained are attributed to the high porosity generated in the analogs upon printing. The generation of voids is found to be inevitable due to the restrictions imposed by the binder jetting printing method, which dictates the usage of non-angular grain particles with a spherical-like morphology, and a grain size distribution with a high fraction of coarse grains. A more detailed discussion with regards to the low friction angle and the impact of the grain morphology on the strength is provided in Sect. 5.

4.3.3 *Failure mode*

Figure 13-a presents the structural appearance observed for TSB after uniaxial and triaxial compression tests from which the type of failure mode was inferred. At low confining pressures, extensional fracturing parallel to the loading direction is dominant characterizing a brittle behavior (case of 0.2, 0.3 and 0.5 MPa). With an increase in confining pressure, well-defined shear bands start to occur, indicating a transitional stage between brittle and ductile behavior (case of 1.5, 2, and 5 MPa). It can be seen that the inclination angle β of the macroscopic failure surface, with respect to the horizontal plane, decreases upon increasing the confining pressure. At high confining pressure (15 MPa for TSB), the sample experiences "barreling" and no visible fractures. This observation is an indication for compaction failure occurring in the samples at confining pressures beyond Mogi's line. The changing failure patterns indicate a transitional behavior from brittle to ductile is clear with increasing confinement, fulfilling the requirement R5.

Table 2 Summary of the calculated strength parameters from conducted laboratory tests on TSA and TSB

	BTS (MPa)	UCS (MPa)	E (GPa)	CI (%)	CD (%)	m_i	C (MPa)	φ (°)
TSA	3.5 (± 0.4)	25.9 (± 0.9)	4.5 (± 0.1)	36 (–)	75 (–)	3.6	7	16
TSB	5.5 (± 0.6)	32.3 (± 3.9)	2.0 (± 0.1)	32 (± 2)	76 (± 3)	3.6	11	15

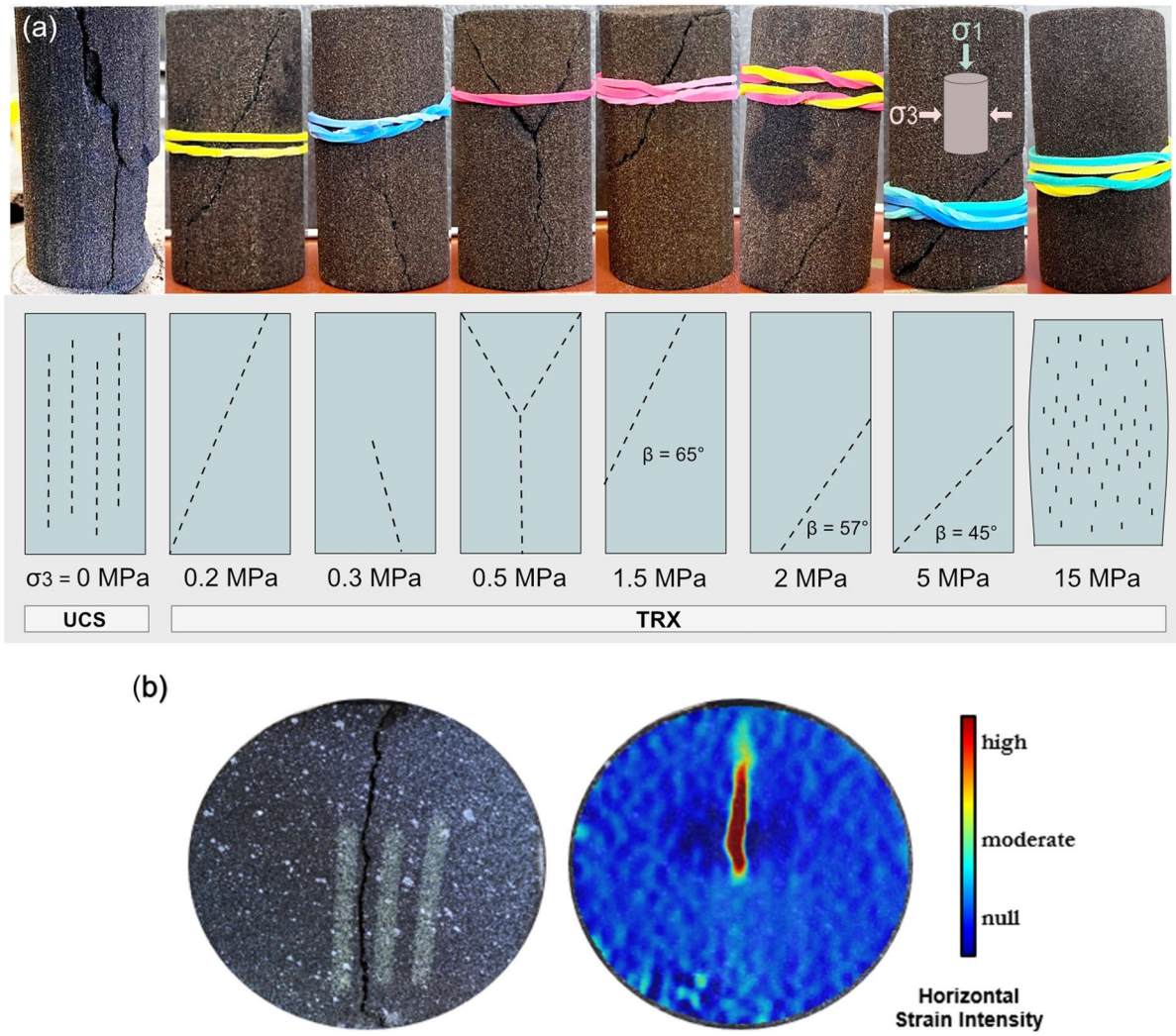

Fig. 13 **a** post-failure images of 3D printed sandstone analogs after uniaxial and triaxial tests with different confining pressures. Visible failure patterns indicate the transition from brittle to ductile behavior as confining increases. **b** Left: post-failure images of 3D printed sandstone analogs after a Brazilian test. Right: horizontal strain field results obtained from DIC analysis done on Brazilian disc

Figure 13-b shows an example of the failure pattern observed in a Brazilian disc after an indirect tensile strength test. Horizontal strain field results obtained from DIC analysis show that the failure in the disc is initiating in an area close to its center, which verifies the validity of a Brazilian test.

5 Thin section analysis

Figure 14-a is an example of a thin section of an untested rock analog viewed under an optical microscope (5×magnification) in plane-polarized light, showing the different structural components, namely:

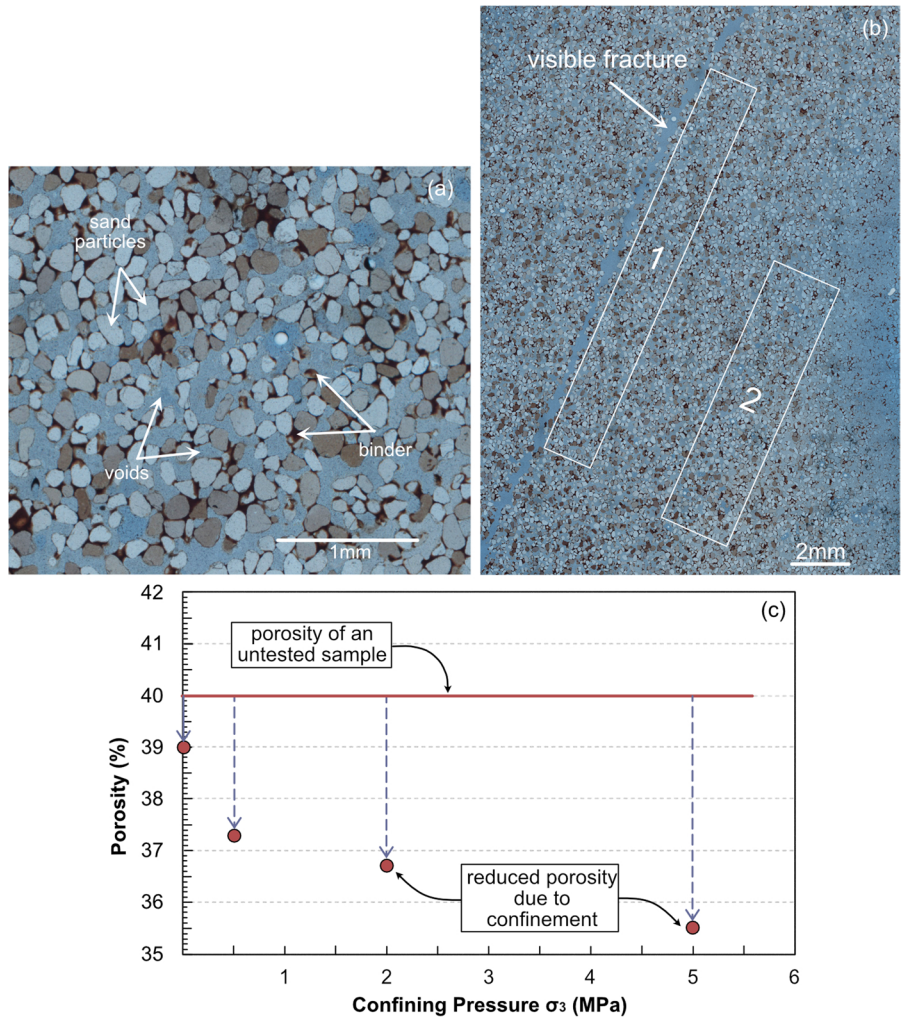

Fig. 14 Microscope view of a thin section extracted from a 3D printed rock sample **a** untested and **b** undergone a TRX test with 5 MPa confinement and had a visible crack. **c** Effect of the applied confinement during compression tests on the porosity of the analogs, measured using thin section method

silica/sand, resins, voids, and binders. It is noticeable that the sand resins have a dominating round morphology, which plays a great role in reducing the friction resistance, hence reducing the friction angle, of the rock analogs undergoing compression and shear stresses (discussed in Sect. 4.3.2). Using ImageJ software for image analysis, a representative elementary area (REA) was found to be 28mm^2 calculated from the untested sample, and used as a fixed area for further analysis. The calculated porosity using ImageJ of an untested sample was 40%, confirming the helium porosity measurement reported earlier.

Thin sections were prepared from samples subjected to confining pressures of 0 MPa (UCS), 0.5 MPa, 2 MPa, and 5 MPa, and viewed under a microscope. The first analysis evaluated the effect of confining pressure applied during TRX tests on the porosity of rock analogs away from the macroscopic fracturing area. As shown in Fig. 14-c, the comparison between the untested sample with a porosity of 40% and the tested samples revealed a porosity reduction induced by confinement, with a decrease of up to 12% in the sample subjected to 5 MPa confinement. This reduction in porosity can be attributed to the morphology of the sand particles, which have a round-like shape, and the initial high void space between them. Therefore, under compression, there is little to no interlocking between the particles, leading to void closure (reduction in porosity), which corresponds to a reduction in volume and reflects the dominating compactional behavior observed under increased confinement. The second analysis was conducted on the TRX sample with confining pressure of 5 MPa. The porosity was evaluated in two different

regions: a) in the proximity of the visible fracture and b) in an area away from the fracture (Fig. 14-b). It was found that the porosity in the region near the fracture was approximately 8% lower than that in the area distant from the fracture, which further proves a compactional failure. Both porosity analyses support the dominating compactional failure occurring at the grain scale of the rock analogs during compression tests and explaining the relatively low frictional strength compared to rocks.

6 Conclusion

This study demonstrates the applicability of the BJP method in producing brittle rock analogs that behave similar to natural rocks, with the main objective of creating specimens that exhibit a very small variability in test results facilitating an unbiased future testing of artificial rock mass containing a fracture network. A thorough analysis on the brittle failure aspects of the rock analogs associated with a comparison to natural brittle rocks is conducted. Two laboratory test series (TSA and TSB) were performed on 3D printed Sand-Furan analogs with different binder saturations under uniaxial/triaxial compression and indirect tensions. Five requirements were defined that needed to be fulfilled for 3D-printed samples to be classified as rock analogs. The requirements include acceptable strength levels and ratio in compression and tension, ability to exhibit brittle damage thresholds, and brittle to ductile transition upon increasing confining pressure.

Laboratory test results indicate that the analogs can reach a UCS of up to 32 MPa, grouped as "moderate strength" according to ISRM classification. Stress–strain curves analysis suggests that the failure process under uniaxial compression is associated with initiation, growth, and coalescence of microcracks; the crack initiation and crack damage thresholds are in the ranges of 30–50% and 70–90% of UCS, respectively, which agrees well with the damage thresholds of natural sedimentary rocks. However, while TSA showed the volumetric strain reversal typically observed for natural sandstones under uniaxial compression, the TSB samples failed to exhibit such behavior. In TSB, bulk volumetric compaction dominates the pre-peak behavior, overshadowing the volumetric strain reversal associated with accumulated damage and dilation.

The ratio between UCS and Young's modulus falls in the range for natural brittle rocks in case of TSA samples. In case of TSB samples, the ratio is at a very lower limit. Both ratios of: UCS to tensile strength, and tensile strength to mode I fracture toughness are well within the range of natural sandstones for the rock analogs. In triaxial compression tests, the analogs captured the transitional behavior from brittle to ductile with increasing confining pressure and the specimen's strength gradually increased. Despite the acceptable strength ranges both in compression and tension, the friction angle and the Hoek–Brown constant (mi) are lower than typically observed in natural rocks. Based on microstructural analyses, this behavior is attributed to the compactional failure occurring during compression tests accompanied by a significant decrease in porosity, i.e. up to absolute 12%, of the analogs undergoing compression tests (UCS and TRX) compared to untested rock analog porosity of 40%. Moreover, it was observed in this study (10–12) % variability among repetitive laboratory tests results, caused by varied printing locations in the printing bed. Therefore, in the future studies, the volume in which the samples are printed will be restricted, decreasing the variability among test results significantly. Overall, the findings of our study confirm the suitability of 3D printed specimens produced using the BJP method for replicating the behavior of natural brittle rocks. This validates performing future laboratory tests on synthetic rocks with embedded discrete fracture networks that contain fully and/or non-persistent joints. 3D printed specimens enable highly controlled laboratory testing and reliable parametric studies, thereby supporting more robust calibration and validation of numerical models. Moreover, they allow researchers to systematically isolate and investigate the influence of individual parameters on the overall strength and deformation behavior of a rock mass.

Author Contribution D.S.: Methodology, Data Curation, Writing – Original Draft, Investigation, Formal Analysis, Data Analysis, Visualization, Project Administration, Literature Review P.H.: Conceptualization, Methodology, Supervision, Funding Acquisition, Project Administration, Validation, Writing – Review & Editing, Critical Review, Literature Review, Data Analysis S.I.: Writing – Review & Editing, Critical Review, Resources G.Z.N.: Writing – Review & Editing, Critical Review, Resources A.J.S.B.: Writing – Review & Editing, Resources L.W.: Writing – Review & Editing, Critical Review,

Resources R.C.: Writing – Review & Editing, Resources F.A.: Conceptualization, Supervision, Funding Acquisition, Critical Review, Writing – Review & Editing, Resources, Project Administration.

Funding Open Access funding enabled and organized by Projekt DEAL. The project is funded by the German Research Foundation (DFG); Project Number: 463538034.

Data Availability No datasets were generated or analysed during the current study.

Declarations

Competing Interests The authors declare no competing interests.

References

Aad EA, Conin M, Deck O, Heib MA (2023) Joint behaviour during shear process using an innovative equivalent geometrical and 3D printing technology. IOP Conf Ser Earth Environ Sci 1124(1):012051. https://doi.org/10.1088/1755-1315/1124/1/012051

Amann F, Button EA, Evans KF, Gischig VS, Blümel M (2011) Experimental study of the brittle behavior of Clay shale in rapid unconfined compression. Rock Mech Rock Eng 44(4):415–430. https://doi.org/10.1007/s00603-011-0156-3

Amann F, Kaiser P, Button EA (2012) Experimental study of brittle behavior of clay shale in rapid triaxial compression. Rock Mech Rock Eng 45(1):21–33. https://doi.org/10.1007/s00603-011-0195-9

Amann F, Ündül Ö, Kaiser PK (2014) Crack initiation and crack propagation in heterogeneous sulfate-rich clay rocks. Rock Mech Rock Eng 47(5):1849–1865. https://doi.org/10.1007/s00603-013-0495-3

ASTM D7012 (2010) ASTM D7012—10 Standard test method for compressive strength and elastic moduli of intact rock core specimens under varying states of stress and temperatures

ASTM (2015) ASTM 52900—2015(E), Standard Terminology for Additive Manufacturing—General Principles—Terminology

ASTM (2021) ASTM International. D3967-16 Standard Test Method for Splitting Tensile Strength of Intact Rock Core Specimens. https://doi.org/10.1520/D3967-16

Barton N (1976) The shear strength of rock and rock joints. Int J Rock Mech Min Sci 13(9):255–79. https://doi.org/10.1016/0148-9062(76)90003-6

Basu A, Mishra DA, Roychowdhury K (2013) Rock failure modes under uniaxial compression, Brazilian, and point load tests. Bull Eng Geol Environ 72(3):457–475. https://doi.org/10.1007/s10064-013-0505-4

RBewickPKaiser2014Discussion on "An Empirical Failure Criterion for Intact Rocks" by Peng et al. (2013)Rock Mech Rock Eng10.1007/s00603-013-0514-4Bewick R, Kaiser P (2014) Discussion on "An Empirical Failure Criterion for Intact Rocks" by Peng et al. (2013). Rock Mech Rock Eng. https://doi.org/10.1007/s00603-013-0514-4

Bewick RP, Kaiser PK, Amann F (2019) Strength of massive to moderately jointed hard rock masses. J Rock Mech Geotech Eng 11(3):562–575. https://doi.org/10.1016/j.jrmge.2018.10.003

Bewick RP, Amann F, Kaiser PK, Martin CD (2015) Interpretation Of UCS Test Results For Engineering Design. 13th ISRM International Congress of Rock Mechanics. https://www.onepetro.org/conference-paper/ISRM-13CONGRESS-2015-209

Bieniawski ZT (1967a) Mechanism of brittle fracture of rock: Part II—experimental studies. Int J Rock Mech Min Sci Geomech Abstr 4(4):407–423. https://doi.org/10.1016/0148-9062(67)90031-9

Bieniawski ZT (1967b) Mechanism of brittle fracture of rock: Part I—theory of the fracture process. Int J Rock Mech Min Sci Geomech Abstr 4(4):395–406. https://doi.org/10.1016/0148-9062(67)90030-7

Blaber J, Adair B, Antoniou A (2015) Ncorr: open-source 2D digital image correlation matlab software. Exp Mech 55(6):1105–1122. https://doi.org/10.1007/s11340-015-0009-1

Brace WF, Bombolakis EG (1963) A note on brittle crack growth in compression. J Geophys Res (1896–1977) 68(12):3709–3713. https://doi.org/10.1029/JZ068i012p03709

Brace WF, Paulding BW, Scholz C (1966) Dilatancy in the fracture of crystalline rocks. J Geophys Res 71(16):3939–3953. https://doi.org/10.1029/JZ071i016p03939

Burley SD, Kantorowicz JD (1986) Thin section and S.E.M. textural criteria for the recognition of cement-dissolution porosity in sandstones. Sedimentology 33(4):587–604. https://doi.org/10.1111/j.1365-3091.1986.tb00763.x

Byerlee JD (1968) Brittle-ductile transition in rocks. J Geophys Res 73(14):4741–4750. https://doi.org/10.1029/JB073i014p04741

Cai M, Kaiser PK, Tasaka Y, Maejima T, Morioka H, Minami M (2004) Generalized crack initiation and crack damage stress thresholds of brittle rock masses near underground excavations. Int J Rock Mech Mining Sci 41(5):833–847. https://doi.org/10.1016/j.ijrmms.2004.02.001

Cook NGW (1965) The failure of rock. Int J Rock Mech Min Sci Geomech Abstr 2(4):389–403. https://doi.org/10.1016/0148-9062(65)90004-5

Deere DU, Miller RP (1966) Engineering classification and index properties for intact rock. illinois univ at urbana dept of civil engineering. https://apps.dtic.mil/sti/citations/AD0646610

Diederichs MS, Kaiser PK, Eberhardt E (2004) Damage initiation and propagation in hard rock during tunnelling and the influence of near-face stress rotation. Int J Rock Mech Min Sci 41(5):785–812. https://doi.org/10.1016/j.ijrmms.2004.02.003

Eberhardt E, Stead D, Stimpson B, Read RS (1998) Identifying crack initiation and propagation thresholds in brittle rock. Can Geotech J 35(2):222–233. https://doi.org/10.1139/t97-091

Eberhardt E, Stead D, Stimpson B (1999) Quantifying progressive pre-peak brittle fracture damage in rock during uniaxial compression. Int J Rock Mech Min Sci 36(3):361–380. https://doi.org/10.1016/S0148-9062(99)00019-4

Eberhardt E (1998) Brittle rock fracture and progressive damage in uniaxial compression. Ph.D. thesis, Department of Geological Sciences, University of Saskatchewan, Saskatoon. http://library.usask.ca/theses/available/etd-10212004-001228/

Ex-One (2014) https://www.exone.com/Admin/getmedia/c8205cfb-ad3a-4b17-bc44-d06c8d773478/2021_X1_Company-Presentation_Metalonly_01_13_1.pdf

Fereshtenejad S, Song J-J (2016) Fundamental study on applicability of powder-based 3D printer for physical modeling in rock mechanics. Rock Mech Rock Eng 49(6):2065–2074. https://doi.org/10.1007/s00603-015-0904-x

Fonseka GM, Murrell SAF, Barnes P (1985) Scanning electron microscope and acoustic emission studies of crack development in rocks. Int J Rock Mech Min Sci Geomech Abstr 22(5):273–289. https://doi.org/10.1016/0148-9062(85)92060-1

Gomez JS, Chalaturnyk RJ, Zambrano-Narvaez G (2018) Experimental investigation of the mechanical behavior and permeability of 3D printed sandstone analogues under triaxial conditions. Transp Porous Media. https://doi.org/10.1007/s11242-018-1177-0

Grasselli G (2001) Shear strength of rock joints based on quantified surface description [EPFL]. https://doi.org/10.5075/epfl-thesis-2404

Hamdi P, Amann F (2020) Evaluating the influence of rock bridge characteristics: rock bridge percentage and spatial location, on the strength of a synthetic rock mass – experimental approach. 54th U.S. Rock Mechanics/Geomechanics Symposium. https://onepetro.org/ARMAUSRMS/proceedings-abstract/ARMA20/All-ARMA20/447493

Hoagland RG, Hahn GT, Rosenfield AR (1973) Influence of microstructure on fracture propagation in rock. Rock Mech 5(2):77–106. https://doi.org/10.1007/BF01240160

Hodder K, Nychka J, Chalaturnyk R (2018) Process limitations of 3D printing model rock. Prog Addit Manuf 3(3):173–182. https://doi.org/10.1007/s40964-018-0042-6

Hodder K, Sanchez-Barra A, Ishutov S, Zambrano-Narvaez G, Chalaturnyk R (2022) Increasing density of 3D-printed sandstone through compaction. Energies 15:1813. https://doi.org/10.3390/en15051813

Hodder K, Ishutov S, Sanchez-Barra A, Zambrano-Narvaez G, Chalaturnyk R (2020) 3D printing of rock analogues in sand: A tool for design and repeatable testing of geomechanical and transport properties. E3S Web Conf, 205, 04014. https://doi.org/10.1051/e3sconf/202020504014

Hoek E, Bieniawski ZT (1965) Brittle fracture propagation in rock under compression. Int J FractMech 1(3):137–155. https://doi.org/10.1007/BF00186851

Hoek E, Brown E (1997) Practical estimates of rock mass strength. Int J Rock Mech Min Sci 34:1165–86. https://doi.org/10.1016/S1365-1609(97)80069-X

Hoek E, Marinos P, Benissi M (1998) Applicability of the geological strength index (GSI) classification for very weak and sheared rock masses. The case of the Athens Schist Formation. Bull Eng Geol Environ 57(2):151–160. https://doi.org/10.1007/s100640050031

Hoek, E. (1968). *Brittle fracture of rock, Chapter 4 in rock mechanics in engineering practice, London: J. Wiley, 99 to 124, Edited by K.G. Stagg and O.C. Zienkiewicz.* www.rocscience.com/hoek/references/H1968a.pdf

Horii H, Nemat-Nasser S (1985) Compression-induced microcrack growth in brittle solids: axial splitting and shear failure. J Geophys Res Solid Earth 90(B4):3105–3125. https://doi.org/10.1029/JB090iB04p03105

Rocscience Inc (2007) Rocscience Inc. RocData user's manual. http://www.rocscience. Com [Computer software]

Jaeger JC, Cook NGW, Zimmerman RW (2007) Fundamentals of rock mechanics (4th ed). Blackwell Pub

Kuruppu MD, Obara Y, Ayatollahi MR, Chong KP, Funatsu T (2014) Isrm-suggested method for determining the mode I static fracture toughness using semi-circular bend specimen. Rock Mech Rock Eng 47(1):267–274. https://doi.org/10.1007/s00603-013-0422-7

Lajtai EZ, Lajtai VN (1974) The evolution of brittle fracture in rocks. J Geol Soc London 130(1):1–16. https://doi.org/10.1144/gsjgs.130.1.0001

Lan H, Martin CD, Hu B (2010) Effect of heterogeneity of brittle rock on micromechanical extensile behavior during compression loading. J Geophys Res. https://doi.org/10.1029/2009JB006496

Li D, Wong LNY (2012) The Brazilian disc test for rock mechanics applications: review and new insights. Rock Mech Rock Eng. https://doi.org/10.1007/s00603-012-0257-7

Martin CD (1997) Seventeenth Canadian geotechnical colloquium: the effect of cohesion loss and stress path on brittle rock strength. Can Geotech J 34(5):698–725

Martin CD, Chandler NA (1994) The progressive fracture of Lac du Bonnet granite. Int J Rock Mech Min Sci Geomech Abstr 31(6):643–659. https://doi.org/10.1016/0148-9062(94)90005-1

Martin CD (1993) The strength of massive Lac du Bonnet granite around underground openings. University of Manitoba

Mellor M, Hawkes I (1971) Measurement of tensile strength by diametral compression of discs and annuli. Eng Geol 5(3):173–225. https://doi.org/10.1016/0013-7952(71)90001-9

Mogi K (1966) Pressure dependence of rock strength and transition from brittle fracture to ductile flow. http://repository.dl.itc.u-tokyo.ac.jp/dspace/handle/2261/12246

Nasseri MHB, Rezanezhad F, Young RP (2011) Analysis of fracture damage zone in anisotropic granitic rock using 3d x-ray ct scanning techniques. Int J Fract 168(1):1–13. https://doi.org/10.1007/s10704-010-9551-0

Nicksiar M, Martin CD (2013) Crack initiation stress in low porosity crystalline and sedimentary rocks. Eng Geol 154:64–76. https://doi.org/10.1016/j.enggeo.2012.12.007

Niu Q, Jiang L, Li C, Zhao Y, Wang Q, Yuan A (2023) Application and prospects of 3D printing in physical experiments of rock mass mechanics and engineering: materials, methodologies and models. Int J Coal Sci Technol 10(1):5. https://doi.org/10.1007/s40789-023-00567-8

Perras MA, Diederichs MS (2014) A review of the tensile strength of rock: concepts and testing. Geotech Geol Eng, 22

Perras MA, Vogler D (2018) Compressive and tensile behavior of 3D-printed and natural sandstones. Transp Porous Media. https://doi.org/10.1007/s11242-018-1153-8

Perras MA, Vogler D (2019) Compressive and tensile behavior of 3D-printed and natural sandstones. Transp Porous Media 129(2):559–581. https://doi.org/10.1007/s11242-018-1153-8

Primkulov B, Chalaturnyk J, Chalaturnyk R, Zambrano Narvaez G (2017) 3D printed sandstone strength: curing of furfuryl alcohol resin-based sandstones. 3D Print Addit Manuf 4(3):149–156. https://doi.org/10.1089/3dp.2017.0032

Salami M (2021) Evaluating the behaviour of rock discontinuities in direct shear under constant normal load and constant normal stiffness boundary conditions using additive manufacturing technology. ERA. https://doi.org/10.7939/r3-cda2-eb36

Sanchez-Barra A, Zambrano-Narvaez G, Chalaturnyk R (2023) An In-depth Analysis of Strength and Stiffness Variability in 3D-Printed Sandstones: Implications for Geomechanics [Preprint]. Engineering. https://doi.org/10.20944/preprints202306.1832.v1

Scholz CH (1968) Microfracturing and the inelastic deformation of rock in compression. J Geophys Res (1896–1977) 73(4):1417–1432. https://doi.org/10.1029/JB073i004p01417

Tapponnier P, Brace WF (1976) Development of stress-induced microcracks in Westerly Granite. Int J Rock Mech Min Sci Geomech Abstr 13(4):103–112. https://doi.org/10.1016/0148-9062(76)91937-9

Tatone BSA (2014) Investigating the evolution of rock discontinuity asperity degradation and void space morphology under direct shear [PhD Thesis]. University of Toronto

Tian Y, Fa-quan Wu, Tian H-M et al (2023) Anisotropic creep behavior of soft-hard interbedded rock masses based on 3D printing and digital imaging correlation technology. J Mt Sci 20(4):1147–1158. https://doi.org/10.1007/s11629-022-7695-9

Ulusay R (Ed.). (2015) The ISRM Suggested Methods for Rock Characterization, Testing and Monitoring: 2007–2014. Springer International Publishing. https://doi.org/10.1007/978-3-319-07713-0

Ündül Ö, Amann F, Aysal N, Plötze ML (2015) Micro-textural effects on crack initiation and crack propagation of andesitic rocks. Eng Geol 193:267–275. https://doi.org/10.1016/j.enggeo.2015.04.024

Vogler D, Walsh SDC, Dombrovski E, Perras MA (2017) A comparison of tensile failure in 3D-printed and natural sandstone. Eng Geol 226:221–235. https://doi.org/10.1016/j.enggeo.2017.06.011

Zhang ZX (2002) An empirical relation between mode I fracture toughness and the tensile strength of rock. Int J Rock Mech Min Sci 39(3):401–406. https://doi.org/10.1016/S1365-1609(02)00032-1

Zhang Y, Suyun N, Zhongming D, Jin H, Jijin Y (2020) Dynamic fracture evolution of tight sandstone under uniaxial compression in high resolution 3d x-ray microscopy. J Pet Sci Eng 195:107585. https://doi.org/10.1016/j.petrol.2020.107585

Zhang K, Li N (2022) A new method to replicate high-porosity weak rocks subjected to cyclic freezing-thawing: sand 3D printing and digital image correlation explorations. Int J Rock Mech Min Sci 157:105174. https://doi.org/10.1016/j.ijrmms.2022.105174

Zhuang D, Ning Z, Chen Y, Li J, Li Q, Xu W (2024) Investigation on mechanical properties regulation of rock-like specimens based on 3D printing and similarity quantification. Int J Min Sci Technol 34(5):573–585. https://doi.org/10.1016/j.ijmst.2024.05.004